Monodisperse Mesoporous Anatase Beads as High Performance and Safer Anodes for Lithium Ion Batteries

Journal:	*Nanoscale*
Manuscript ID	NR-ART-07-2015-004432.R1
Article Type:	Paper
Date Submitted by the Author:	17-Sep-2015
Complete List of Authors:	Rodriguez, Erwin; The University of Melbourne, School of Chemistry; CSIRO, Manufacturing Flagship Chen, dehong; Melbourne University, School of Chemistry Hollenkamp, Anthony; Minerals Building, CSIRO Energy Technology Cao, Lu; The University of Melbourne, School of Chemistry Caruso, Rachel; The University of Melbourne, ARC Future Fellow; CSIRO, Materials Science and Engineering

Nanoscale

ARTICLE

Monodisperse Mesoporous Anatase Beads as High Performance and Safer Anodes for Lithium Ion Batteries†

Received 00th January 20xx,
Accepted 00th January 20xx

DOI: 10.1039/x0xx00000x

www.rsc.org/

Erwin F. Rodriguez,[a,b] Dehong Chen,*[a] Anthony F. Hollenkamp,[c] Lu Cao[a] and Rachel A. Caruso*[a,b]

To achieve high efficiency lithium ion batteries (LIBs), an effective active material is important. In this regard, monodisperse mesoporous titania beads (MMTBs) featuring well interconnected nanoparticles were synthesised, and their mesoporous properties were tuned to study how these affect the electrochemical performance in LIBs. Two pore diameters of 15 and 25 nm, three bead diameters of 360, 800 and 2100 nm, and various annealing temperatures (from 300 to 650 °C) were investigated. The electrochemical results showed that while the pore size does not significantly influence the electrochemical behaviour, the specific surface area and the nanocrystal size affect the performance. Also, there is an optimum annealing temperature that enhances electron transfer across the titania bead structure. The carbon content employed in the electrode was varied, showing that the bead diameter strongly influences the minimal content of the conductive carbon required to fabricate the electrode. As a general rule, the smaller the bead diameter, the more carbon was required in the electrode. A large energy capacity and high current rate performance was achieved on the MMTBs featuring high surface area, nano-sized anatase crystals and well-sintered connections between the nanocrystals. The high stability of these mesoporous structures was demonstrated by charge/discharge cycling up to 500 cycles. The MMTBs retained more than 80 % of the initial capacity, indicating an excellent performance.

Introduction

Currently lithium ion batteries (LIBs) have been widely used in many portable device and power tool industries; the corresponding market is expected to reach ~US$38 billion by 2020.[1] Most of these commercial LIBs employ carbon materials, most notably graphite mineral, as the anode.[2] Since the carbon materials operate at low voltage (0-0.25 V *vs* Li/Li$^+$), lithium plating can occur on the carbon surfaces especially during fast charge operation, resulting in the formation of lithium dendrite that grows across the electrolyte. This can lead to short circuits and uncontrollably energetic chemical reactions within the battery, and subsequently end up with a thermal runaway (fire or explosion).[3] Although the growth of lithium dendrites can be suppressed by forming a solid-electrolyte interphase (SEI) layer on the graphite surface during the initial intercalation of lithium,[4, 5] this SEI layer is thermally unstable and can decompose at a temperature as low as 60 °C. Hence it could trigger a continuous exothermal reaction within the device and result in thermal runaway. This concerning characteristic of LIBs employing carbon-based anodes has been recognised as one of several technological barriers that hinder LIBs deployment for automobile and smart-grid applications.[2, 4, 6]

To fabricate safer batteries for practical energy storage applications, anode materials with enhanced safety are in high demand. The desirable anode material should possess a potential above 0.8 V *vs* Li/Li$^+$ to prevent the lithium dendrite growth and the reduction of the electrolyte.[6] From a range of anode candidates, titanium-based materials, especially anatase titania, spinel $Li_4Ti_5O_{12}$ and TiO_2-B (bronze-type), have been verified as the most promising candidates for such purpose due to their relatively high potential (>1.5 V *vs* Li/Li$^+$), significantly better structural and thermal stabilities, excellent rate capacity and long cycle and calendar lives.[6-9] Moreover, to maximise the volumetric energy density of the battery for practical applications, control of the morphology and grain size of these materials is also an important factor for consideration.[10, 11] Among diverse morphologies, spherical micrometre-sized particles composed of nanocrystals are highly desirable because of their good mobility and high packing density. This is beneficial for the fabrication of uniform and close-packed particulate networks in the electrode,[12-16] thus imparting enhanced volumetric energy density and rate capability to the batteries.

Although some efforts have been devoted to the fabrication of mesoporous spherical titania particles as safer anode materials for LIB application previously,[11, 17-21] to our best knowledge, no systematic studies addressing the effects of diverse physical

---

[a] *Particulate Fluids Processing Centre, School of Chemistry, The University of Melbourne, Victoria, 3010, Australia. E-mail: rcaruso@unimelb.edu.au, dehongc@unimelb.edu.au*
[b] *Manufacturing Flagship, The Commonwealth Scientific and Industrial Research Organisation (CSIRO), Clayton, VIC 3168, Australia*
[c] *Energy Flagship, The Commonwealth Scientific and Industrial Research Organisation (CSIRO), Clayton, VIC 3168, Australia*

† Electronic Supplementary Information (ESI) available: See DOI: 10.1039/x0xx00000x

properties (e.g. porosity, grain size and annealing temperature) on the electrochemical performance of the resulting LIBs have been studied. Moreover, fair comparison among the reported results is difficult because of the variables in the half-cell fabrication, i.e., the loading amount of active materials, conductive additives, electrolytes and cell format. In this study, monodisperse mesoporous titania beads (MMTBs) with tuneable physical properties, including pore diameter, specific surface area, bead diameter, grain size and anatase nanocrystal connectivity were fabricated as anode candidates for LIBs using a facile sol-gel and solvothermal process. The effects of these physical properties on the electrochemical behaviour of the LIB were investigated in detail. The amount of conductive carbon additive employed in the electrode preparation was also studied for the MMTBs with different diameters to understand how the electrode composition affected the electrochemical performance of the resulting anodes.

Experimental section

Titania bead fabrication and characterisation

Titania beads with different diameters (360, 800 and 2100 nm) and pore diameters (15 and 25 nm) were prepared using the following chemicals: Titanium (IV) isopropoxide (TIP, 97 % Sigma-Aldrich), hexadecylamine (HDA, 90 % Sigma-Aldrich), ethanol (99.5% Chem-Supply), 1-butanol (99.8% Chem-Supply), potassium chloride (AR BDH), ammonia solution (25 % Merck) and Milli-Q water (18.2 MΩ cm). The detailed procedure for fabricating the amorphous precursor beads has been published.[22-24] The 360 nm beads were prepared by increasing the water content used in the sol-gel synthesis, whereas the 2100 nm beads were prepared using 1-butanol as solvent. [22-24]
To obtain crystalline mesoporous anatase beads with different pore sizes, the precursor beads were solvothermally treated in the presence of a 0.45 M ammonia solution at 160 °C for 16 h (25 nm pore-size) or in the absence of ammonia at the same temperature (15 nm pore-size).[22, 23] The product was washed, dried and finally annealed under an air atmosphere for 2 h at different temperatures as later indicated.

The morphology of the samples was observed using a field emission environmental scanning electron microscope (SEM, FEI Quanta 200F) under low vacuum mode without any sputter coating pretreatment of the samples. The porosity and structure within the bead samples were investigated using a FEI Tecnai F20 transmission electron microscope (TEM) at 200 kV. Powder X-ray diffraction (XRD) measurements were conducted on a Bruker D8 Diffractometer with Cu Kα radiation in the range from 5 to 80°. Nitrogen gas sorption measurements were collected using a Micromeritics Tristar 3000 surface area and porosity analyser. Prior to the measurement, the samples were degassed at 150 °C for 18 h on a vacuum line. The specific surface area of the samples was calculated by a standard multipoint Brunauer-Emmett-Teller (BET) method using the adsorption data in the P/P_0 range from 0.05 to 0.20. The pore diameter distribution of the samples was determined using the Barett-Joyner-Halenda (BJH) model applied to the adsorption branch of the isotherms. The X-ray photoelectron spectrometer (XPS) data were recorded on a VG ESCALAB 220i-XL spectrometer (UK) equipped with a twin crystal monochromated Al K_α X-ray source.

Electrode preparation and electrochemical characterisation

The working electrodes were prepared by mixing MMTBs (the active material), carbon black (~40 nm, Super P® as conductive material), and 6 wt% polyvinylidene difluoride dissolved in N-methyl-2-pyrrolidone (PVDF and NMP were both from Sigma-Aldrich and used as a binder). The final PVDF content within the electrode for all experiments was maintained at 10 wt%. The amount of conductive carbon was kept constant at 10 wt% for most experiments, but varied for some specific experiments as detailed later. To obtain reproducible electrochemical measurements, it was necessary to prepare a homogeneous suspension of MMTBs in ethanol. This was achieved by sonicating the MMTBs agglomerates in ethanol for 1 h until the beads were thoroughly suspended in the solution. Carbon black was then added, and the mixture was sonicated for an additional half hour. The ethanol was evaporated under low pressure at ~55 °C, and acetone was added (~10 mL per half gram) before the suspension dried entirely at ~40 °C. The resulting powder was further dried at 100 °C under atmospheric pressure for 1 h. The dry powder and PVDF pre-dissolved in NMP (6 wt% PVDF) were mixed, adding NMP (2 mL per 0.5 g of powder) to prepare a viscous slurry for making electrodes. The resulting mixtures were mechanically stirred at 2000 rpm for 1 h with a rectangular 4-bladed propeller. The slurry was cast on a pre-sanded aluminium foil (current collector, 30 μm in thickness), then dried and finally pressed with a roller. The electrodes were dried at 100 °C overnight in an oven under vacuum. The loading of the active material was between 0.33 and 0.83 mg cm^{-2}. Half coin cells (type CR2032) were assembled in an argon-filled glove box with a lithium metal counter electrode, polyethylene as the membrane separator (SOLUPOR, 5P09B; Lyndall), and $LiPF_6$ (1 M) in a solution of ethylene carbonate:dimethyl carbonate:diethyl carbonate (EC:DMC:DC, volume ratio) = 1:1:1 as electrolyte. The assembled coin cells sat for at least 24 h before being tested. Galvanostatic charge/discharge tests in a voltage range from 1.0 to 3.0 V were carried out at various current densities (1 C = 168 mA g^{-1}) by using a battery tester (MACCOR series 4000). The electrochemical impedance spectroscopy (EIS) measurements, at a bias potential of 1.8 V after 45 galvanostatic cycles, were carried out by applying a sine wave with amplitude of 10 mV over the frequency range from 100 kHz to 0.1 Hz by using a frequency response analyser (Solartron 1255B).

Results and discussion

Since electrochemical performance of the active material for LIBs depends on their morphological and physical properties, MMTBs featuring systematic variations in: (i) pore diameter (15 and 25 nm), (ii) bead diameter (360, 800, and 2100 nm) and (iii) intercrystal connections (by sintering at diverse temperatures) were investigated. Additionally, the conductive carbon content in electrodes was also investigated to elucidate how it influences the electrode performance.

The synthesised MMTBs presented a higher packing density compared to the Evonik (Degussa) P25 nanoparticles owing to the intra-particle binding in the mesoporous structure and their uniform spherical morphology (Fig. S1). It is worth mentioning that the homogeneity of the films (Fig. S2 and S3a) and the loading of the active materials (Fig. S3b) were optimised to minimise the variation of the electrochemical results, as explained in the supplementary information.

Effect of mesopore size within the beads

To study the influence of the mesopore size within the beads on the electrochemical behaviour of the electrodes, MMTBs with an average pore diameter of 15 and 25 nm were fabricated. These MMTBs had an average diameter of 800 nm and were annealed at 500 °C for 2 h in air. Nitrogen gas sorption isotherms and corresponding pore diameter distributions of the 800 nm MMTBs are given in Fig. 1a and 1b. Both MMTBs showed type IV isotherm curves with an obvious hysteresis loop, indicating the presence of mesopores (Fig. 1a). The BJH pore diameter distributions extracted from the adsorption branches of the isotherms present narrow Gaussian distributions centred at either 15 or 25 nm (Fig. 1b). The BET surface area for the 15 and 25 nm pore-sized beads was measured as 110 and 85 m^2 g^{-1}, respectively. On the basis of the BET surface area, the diameter of the titania nanocrystals can be estimated using the following equation assuming the primary nanocrystals have a spherical shape:

$$d = {}^{6}/_{(\rho * S_{BET})}$$

where d refers to the average crystal diameter, ρ is the density of anatase (3.9 g cm^{-3}), and S_{BET} refers to the BET surface area. The estimated crystal size for the 15 and 25 nm pore-sized beads is 14.0 and 18.1 nm, respectively. Both MMTBs present anatase as the single phase according to the corresponding XRD patterns (Fig. S4a and JCPDS card No. 21-1272). The crystal size estimated by applying the Scherrer equation to the (101) peak is 13.9 and 15.8 nm for the 15 and 25 nm pore-sized beads, respectively, in agreement with the estimated values from the BET surface area. Both samples were monodisperse beads (Fig. 2a) having an average diameter of 800 nm (Fig. S4b), and were composed of nanocrystals with different sizes (Fig. 2b-e). As clearly illustrated in the corresponding SEM and TEM images (Fig. 2b-e), the 25 nm pore-sized beads possess a relatively larger primary crystal size than the 15 nm pore-sized ones. This result is consistent with the estimations derived from both the XRD and BET surface area analysis. The corresponding TEM images (ultramicrotomed sections shown in Fig. 2c and 2e) demonstrate uniform mesoporosity throughout the whole spherical structure. The physical properties of the beads are summarised in Table 1.

Table 1. Physical properties of the 800 nm anatase beads annealed at 500 °C with different mesopores.

Diameter (nm)[a]	Crystal size[b] (nm)	Surface area (m^2 g^{-1})	Pore diameter[c] (nm)
800	15.8	85	25
800	13.9	110	15

[a] The bead diameter distributions are presented in Fig. S4b.

[b] Determined by applying the Scherrer equation to the (101) anatase peak of the corresponding XRD pattern.

[c] Calculated using the Barrett-Joyner-Halenda (BJH) model on the N_2 adsorption branch.

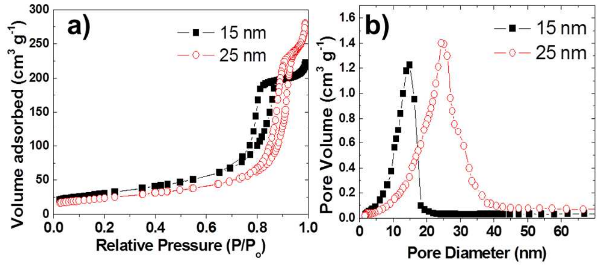

Fig. 1. a) Nitrogen gas sorption isotherms and b) pore diameter distributions of the 800 nm anatase beads featuring 15 and 25 nm mesopores. Both beads were annealed at 500 °C for 2 h in air.

The differences in pore size, BET surface area and crystal size, of the previous samples are reflected in the electrochemical behaviour. First, the galvanostatic cycle at low current rate (0.2 C, Fig. 3a) for both pore-sized beads can be separated into three regions for the insertion/extraction of lithium (labelled as I to III in Fig. 3a).[25-27] For the lithium insertion (discharge curve in Fig. 3a) the regions are described as follows.

Region I: The region before reaching the constant voltage at ~1.77 V can be attributed to homogeneous Li insertion into the bulk anatase, up to the solid-solution limit of Li in tetragonal TiO_2.[27, 28] The orthorhombic phase of the lithiated Li_xTiO_2 starts to appear at about x = 0.05;[28] however, the exact value is still controversial.[28, 29]

Region II: A typical two-phase reaction[30] with a constant plateau of ~1.77 V is present in this region. The lithium randomly inserts into around half of the interstitial octahedral sites of the bulk anatase in a typical Faradaic reaction.[25, 27, 31] Therefore, around half of the maximum theoretical capacity is reversible in the bulk anatase.[31]

Region III: The slope after the plateau, from ~1.77 V to 1 V, belongs to the energy capacity accumulated on the surface region of the anatase nanocrystals.[32-34] This capacity contribution arises from both the pseudocapacitance at the interface and the double layer effect.[34]

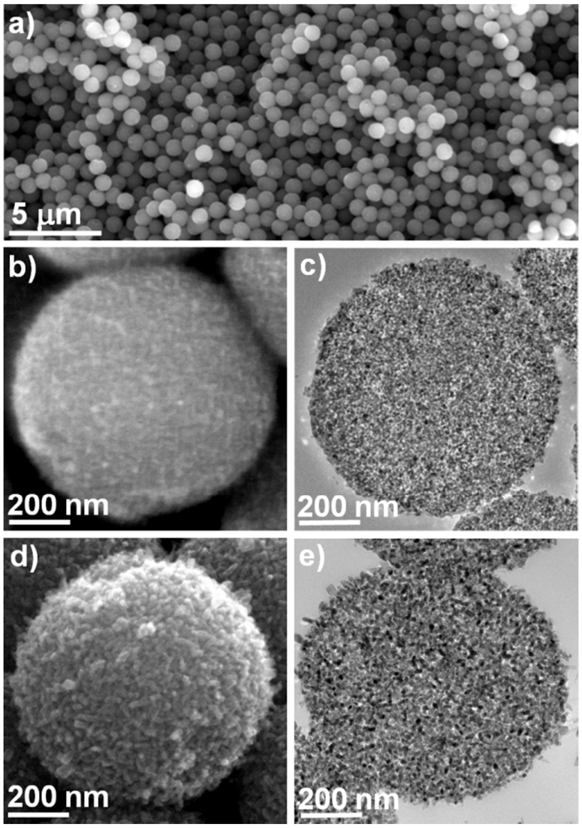

Fig. 2. SEM (a, b, and d) and TEM (c and e, ultramicrotomed sections) images of the 800 nm anatase beads featuring 15 nm (a,b and c) and 25 nm (d and e) mesopores. Both beads were annealed at 500 °C for 2 h in air. Note: All the SEM images were taken without metal sputter coating pretreatment of the samples.

Although the overall discharge capacity of the 15 and 25 nm pore-sized beads was different (233 and 208 mAh g^{-1}, respectively, Fig. 3a), the bulk capacities (Regions I and II) of both samples were similar in value. At low current rate it is expected that the same amount of lithium is able to diffuse into the octahedral sites of the bulk anatase. However, for the surface capacity (Region III), the 15 nm pore-sized beads achieved a larger surface capacity (~89 mAh g^{-1}) than the 25 nm pore-sized beads (~69 mAh g^{-1}), which is in direct proportion to the specific surface areas of the corresponding MMTBs (110 and 85 m^2 g^{-1}, respectively). Thus the MMTBs with 15 nm pore size delivered an excellent capacity of 233 mAh g^{-1} at a rate of 0.2 C mainly due to the improved surface capacity. At high current rates, the influence of the surface area was less significant than that of the crystal size. The rate capabilities of the 15 and 25 nm pore-sized beads, as shown in Fig. 3b, display a similar falling tendency when increasing the current rate. At a high current rate of 40 C, the contribution of the bulk and surface capacities were significantly different. The overall capacities at 40 C of the 15 and 25 nm pore-sized beads were 63 and 46 mAh g^{-1}, respectively, and the difference was mainly in the bulk capacity (Regions I and II), which is much larger for the 15 nm pore-sized beads (Fig. 3c). As the crystal size of 15 nm pore-sized beads (~14 nm) is smaller than that of the 25 nm pore-sized beads (~16 nm), the path length of the Li diffusion is reduced for the former, thus increasing the bulk lithium capacity storage at high current rate. At a high current of 20 C, an impressive capacity of ~110 mAh g^{-1} can be readily achieved on the 15 nm pore-sized beads as a result of the small crystal size, which effectively shortens the diffusion length of the Li ions.

On the other hand, the polarisation of the lithium insertion/extraction plateaus at increasing current rate is not noticeable until 5 C (Fig. 3f). This low polarisation indicates that beyond 5 C there were kinetic limitations from the electron charge transfer and the Li diffusion into the material. The polarisation at high current rates (>5 C) for the synthesised MMTBs is significantly lower when compared with the high-performing materials reported previously,[11, 35] owing to the presence of abundant mesopores, high surface area and the nano-sized primary crystals of the MMTBs.

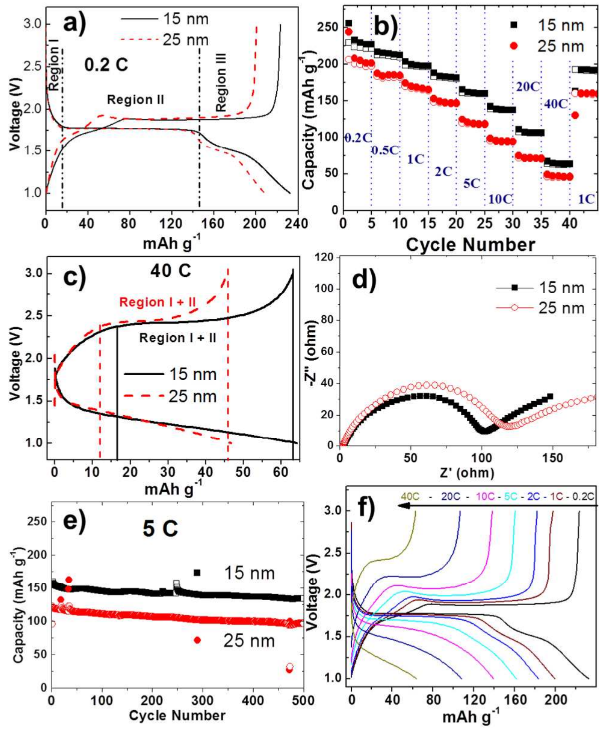

Fig. 3. Electrochemical performance of the electrodes fabricated using 800 nm anatase beads featuring 15 and 25 nm mesopores. a) Galvanostatic voltage profiles at 0.2 C (2nd cycle), b) current rate capabilities (The solid and open symbols represent the discharge and charge capacities, respectively), c) galvanostatic voltage profiles at 40 C rate, d) impedance plane plots at bias voltage of 1.8 V, e) cycling performance at 5 C rate recorded after the 45 cycles of the rate capability test, and f) galvanostatic voltage profiles of the 15 nm pore-sized anatase beads.

In order to gain more insight into the influence of the pore size, EIS measurements were carried out. The tested cells were held at 1.8 V where the semicircle is more defined; the components of the Nyquist plot are more fully explained following Fig. S5, which shows the Nyquist plots for various bias voltages and the equivalent circuit of the cell. The estimated impedance parameters from the equivalent circuit are presented in Table S1, and the lithium ion diffusion coefficients calculated at low frequencies are presented in

Table S2. Even though both EIS spectra (Fig. 3d) are basically similar in shape, a slight reduction in the magnitude of the depressed semicircle is observed for the smaller mesopore size, suggesting that there is a decrease in the charge transfer resistance for the 15 nm mesopore. The fact that the solution resistance at high frequencies is almost equal for both samples (Fig. 3d) indicates that either the pore sizes are too small for the EIS test at these high frequencies or the difference in pore size (15 to 25 nm) does not influence the diffusion resistance of the Li^+ ions inside the bead. Porous anatase particles possessing 5.4-8.0 nm mesopores have previously been investigated,[11, 18, 26, 36] and high current rate capabilities were achieved on these materials using similar electrolytes as reported in this study, suggesting that even smaller mesopores (less than 15 nm) do not hinder the electrochemical performance.

Both pore-sized beads retained stability over a long cycle period (Fig. 3e), which is ascribed to their unique, stable mesoporous structure, nano-sized crystals, and the high surface area. At a 5 C rate, the percentage retention after 500 cycles for the 15 and 25 nm pore-sized beads was 85 and 81 %, respectively, and the Coulombic efficiencies for both samples were close to 100 % for all cycles, indicating a superior structural stability of the MMTBs. As presented in Fig. S6, the spherical morphology of the MMTBs did not change substantially after the 500 charge/discharge cycles, further indicating their excellent structural stability.

Effect of the bead diameter and percentage of conductive carbon

To investigate the influence of the bead diameter on the electrochemical performance, MMTBs with varied diameters (360, 800 and 2100 nm) but consistent mesopore size (15 nm) were synthesised.[22-24] All these MMTBs were annealed at 500 °C for 2 h under an air atmosphere. SEM images present in Fig. 4a, 4c and 4e revealed that these three samples have well-defined spherical shapes and monodisperse size distributions (Fig. S7a). XRD patterns of these three beads (Fig. S7b) are in good agreement with the standard pattern of anatase (JCPDS card No. 21-1272), and the crystal size estimated from the peak broadening was ~14.0 nm for these three samples. Nitrogen sorption isotherms of the three samples present type IV isotherms with obvious hysteresis loops, indicating the presence of mesoporosity (Fig. S8a). The Gaussian BJH pore diameter distributions obtained from the adsorption branches of the isotherms gave a pore size centred at ~15 nm for these three beads (Fig. S8b). The BET specific surface area increased from 107 to 117 m^2 g^{-1} (Table 2) as the bead diameter increased from 360 to 2100 nm. Assuming a spherical shape for the primary particles, the crystal size estimated from the BET surface area was between 13.0 to 14.0 nm, which is in a good agreement with the XRD estimation. In brief, these three beads present the same anatase phase, comparable crystal size and similar mesoporosities (Table 2).

Table 2. Physical properties of the monodisperse mesoporous anatase beads with diverse diameters (360, 800 and 2100 nm)

Nominal diameter (nm)[a]	Crystal size (nm)[b]	BET surface area (m^2 g^{-1})	Pore diameter (nm)[c]
360	14.0	107	15
800	13.9	110	15
2100	14.0	117	15

[a] The diameter distribution of the beads is presented in Fig. S7a.

[b] Determined by applying Scherrer equation to the (101) anatase peak of the corresponding XRD pattern.

[c] Calculated using the BJH model on the N_2 adsorption branch.

The electrochemical behaviour when varying the diameter of the beads and keeping the other variables constant showed no differences in capacity at low currents (0.2 – 0.5 C), whereas upon increasing the current rate the electrochemical performance of materials varied. First, the overall morphology of the electrodes (10 wt% conductive carbon, Fig. 4b, d, f and g) shows that the beads were irregularly packed and their spherical morphology was kept after the electrode preparation. The distribution of carbon was uneven for the different diameter beads, but the reproducibility of the coin cells was satisfactory. As previously described, three separate regions for lithium insertion/extraction can clearly be distinguished in the galvanostatic charge/discharge profiles. The discharge profiles at low current (0.2C, Fig. 5a) showed that the bulk capacities (region I and II) of the three beads are close in value because the three samples present the same anatase phase, as well as similar crystal sizes. Moreover, the surface capacities (region III) for the three samples are also similar in value due to the approximately equal BET surface areas. The reversible overall discharge capacity at this low current was 231, 232, and 226 mAh g^{-1} for the 360, 800 and 2100 nm MMTBs, respectively. Upon increasing current rate for the three electrodes (10 wt% of carbon, Fig. 5b), the discharge capacity fades rapidly for the smallest diameter beads (360 nm) followed by the largest diameter beads (2100 nm) and then the intermediate sized beads (800 nm). The capacity of the latter was sustained even at 40 C, retaining 63 mAh g^{-1}. The Nyquist plot of the three samples in Fig. 5c shows that at high frequency the real intercept related to the electrolyte resistance has a close value for the three samples, which is consistent with the fact that the properties of the electrolyte solution do not change. At high and medium frequencies, the charge transfer resistance shows its lowest value for the 800-nm-diameter beads (Table S1). The 360-nm-diameter beads, on the other hand, presented the highest charge transfer resistance, even though this sample has similar mesoporous properties, the same TiO_2 phase and equal carbon content, compared to the other electrodes. Therefore, the 800-nm-diameter beads delivered a higher electrochemical performance than the 360-nm-diameter beads, as demonstrated by the galvanostatic and EIS tests. At low frequencies, the estimated diffusion coefficients of Li ion are in the same order of magnitude with slightly lower value for 360-nm-diameter beads (Table S2).

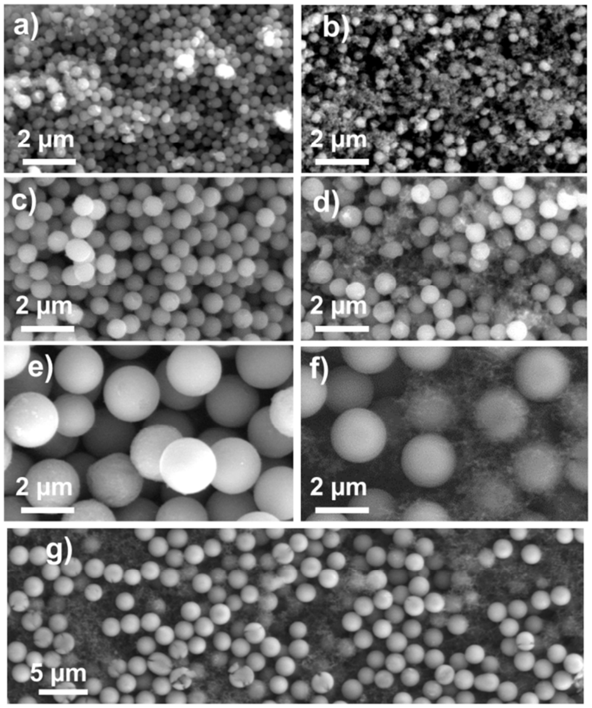

Fig. 4. SEM images of the as-synthesised anatase beads (a, c and e) and those mixed with 10 wt% of conductive carbon in the fabricated electrodes (b, d, f and g): (a, b) 360, (c, d) 800, and (e, f, g) 2100 nm in diameter. All these beads have the same mesopore diameter (15 nm) and have been annealed at 500 °C for 2 h in air. Note: all the SEM images were taken without metal sputter coating pretreatment of the samples.

To investigate the cause for the poor performance of electrodes prepared from the 360 nm beads, the carbon content was increased from 10 to 15 then 30 wt%. As shown in Fig. 5d, at increasing current rate the electrochemical performance improved with each increase in carbon content. The electrode with 30 wt% of carbon outperformed the 800 nm beads with a 73 mAh g^{-1} capacity at 40 C rate. The EIS measurements for the three carbon contents show that the charge transfer resistance gradually fell with each increase in the carbon content (Fig. 5e), explaining the enhancement in the current rate capability. The reduction in this component of impedance is, however, offset partly by a growth in the Warburg (diffusion) component. In other experiments with the electrode of 800-nm-diameter beads and 25 nm pore diameter, the carbon content was reduced from 10 to 5 wt% (Fig. S9a), resulting in greater capacity fading upon increasing currents that was similar to the 360-nm-diameter beads with 10 wt% carbon. The EIS measurements for the 800-nm-diameter beads at different carbon content (Fig. S9b) also show that the charge transfer resistance increases as the carbon content decreases. These results suggest that 10 wt% of carbon in the 800-nm-diameter beads was sufficient to preserve an electronic network between the beads, whereas there was insufficient carbon to maintain the electronic connections in the 360-nm-diameter bead electrode. Therefore, in order to achieve the optimum electrochemical performance of a mesoporous material with the minimal content of carbon, the amount of carbon required to provide the electronic connectivity increases when decreasing the average diameter of the mesoporous material. Considering that the volume occupied by a single 2100-nm-diameter bead could incorporate ~138 single randomly ordered 360-nm-diameter beads, and these smaller beads have ~3.7 times more outer surface area than the single 2100-nm bead, much more carbon is needed to provide the electronic network for the small beads simply because of the larger outer surface area. For instance, to keep the electronic connections in 6-nm-anatase particles, up to 45 wt% of conductive additive was required to prepare a high-performing electrode.[25, 28] On the other hand, the high stability of the MMTBs (360 nm diameter) with 30 wt% of carbon upon lithium insertion/extraction was demonstrated by cycling the electrode up to 500 cycles at 5 C rate (Fig. 5f). The capacity retention was ~81 %, and the Coulombic efficiencies for all cycles were close to 100 %.

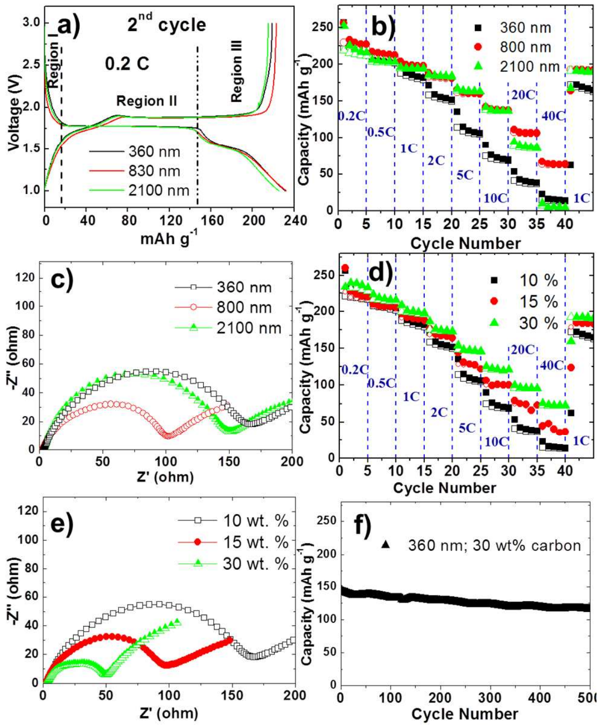

Fig. 5. Electrochemical performance of the electrodes fabricated using 360, 800 and 2100 nm anatase beads and mixed with 10 wt% conductive carbon (a-c): a) Galvanostatic voltage profiles at 0.2 C (2nd cycle), b) current rate capabilities at diverse C rates, and c) impedance plane plots at 1.8 V bias voltage. Electrochemical performance of the electrodes prepared using 360 nm anatase beads with 10, 15 and 30 wt% of conductive carbon (d-e): d) current rate capabilities, e) impedance plane plots at 1.8 V bias voltage. f) Cycling performance at 5 C rate of the electrode fabricated using 360 nm beads mixed with 30 wt% conductive carbon (after the 45 cycles of the current rate capability test).

Despite some qualitative similarities in the impedance (Fig. 5c) for the beads with 2100 and 800 nm diameter containing 10 wt% of carbon, both samples achieved particularly distinct electrochemical performances at high current rate. The discharge capacity for both diameter beads remained quite similar until 10 C (Fig. 5b), but above this current rate the capacity of the 2100-nm-diameter beads decreased rapidly, recording nil at 40 C. While the magnitude of charge transfer resistance of both bead diameters is similar, small yet obvious differences in the shape of the depressed semicircle indicate that the charge transfer resistance is composed of a combination of components. As just discussed, the electrochemical performance of the smallest beads is dominated by the properties of the inter-bead regions such that the addition of more conductive carbon has a dramatic effect. Additionally, inter-bead impedance is much less a factor for the largest beads, whereas intra-bead conductivity is clearly a more dominant issue, simply based on a consideration of the relative bead volumes. Presumably, the main factor here is the resistance of the network of nanoparticles. To clarify this phenomenon, the MMTBs were annealed at higher temperatures to increase the degree of sintering between the internal interfaces/boundaries of the primary particles and thus increase the electronic conductivity.

Influence of the annealing temperature

Large beads with 800 or 2100 nm diameter were used to investigate the influence of annealing temperature on the electrochemical behaviour of LIBs. Increasing the annealing temperature from 500 to 600 °C, the 2100 nm beads with 15 nm pore size did not significantly change in morphology and mesoporosity. For the sample annealed at 600 °C, the XRD pattern (Fig. S10) can be ascribed to anatase, and the estimated crystal size from the peak broadening was ~15 nm, which is slightly higher than 14 nm of the sample annealed at 500 °C. The nitrogen gas sorption isotherm also revealed a typical type IV isotherm with a hysteresis loop, indicative of a mesoporous structure (Fig. S11a), and the BJH pore diameter distribution (Fig. S11b) shows a narrow Gaussian curve centred at ~16 nm which is slightly larger compared with the 15 nm of the 500 °C sample (annealing the sample at a temperature higher than 600 °C significantly increased the pore size of the beads as shown in Fig. S11b). The BET surface area is 105 m^2 g^{-1} when annealed at 600 °C, which is smaller than that of the sample annealed at 500 °C (117 m^2 g^{-1}), and the primary particle size estimated from the BET surface area of the sample annealed at 600 °C is ~15 nm, which is consistent with the XRD estimation.

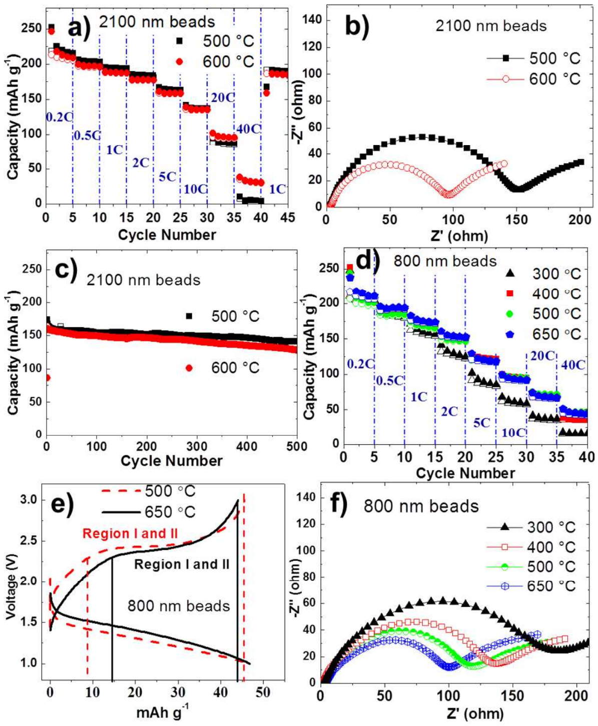

Fig. 6. Electrochemical performance of the electrodes fabricated using 2100 nm anatase beads with 15 nm mesopores and annealed at 500 and 600 °C, respectively (a-c): a) Current rate capabilities at various C rates, b) impedance plane plots at 1.8 V bias voltage, and c) cycling capability at 5 C rate. Electrochemical performance of the electrodes fabricated using 800 nm beads with 25 nm mesopore and annealed at various temperatures (d-f): d) current rate capabilities at diverse C rates, e) charge/discharge profiles at 40 C rate for the samples annealed at 500 and 650 °C, and f) impedance plane plots at 1.8 V bias voltage.

The electrochemical performance of the MMTBs annealed at a temperature higher than 500 °C shows an improvement, as demonstrated by the galvanostatic tests at increasing current densities and EIS measurements (Fig. 6). Even though the discharge capacities at low current rate (0.2 C) for the samples annealed at 500 and 600 °C gave almost the same value (225 and 218 mAh g^{-1}, respectively) owing to the similar surface areas and crystal sizes of both samples, the capacity retention at high currents for the 600 °C sample is considerably improved (Fig. 6a). For instance, the capacity retention at 40 C rate was increased from nearly nil to 14% (32 mAh g^{-1}; based on the 2nd cycle) by increasing the temperature from 500 to 600 °C, clearly demonstrating the improvement of the performance. This improvement is less visible at low current rates, e.g., the retention at 20 C rate for the beads annealed at 500 and 600 °C is only improved from 38 to 44 %, respectively. Similarly, the impedance spectra in the region of middle frequencies reveals that the charge transfer resistance reduces when the annealing temperature increases, as demonstrated by the significant fall of the depressed semicircle (Fig. 6b and Table S1). Since the semicircles are also related to the charge transfer resistance between the particles in the boundaries,[37] we can infer that the resistance was reduced by enhancing the conductivity between the crystal interfaces, which also enhances the electrochemical performance at high current rate. Moreover, Saravanan et al.[11] suggested that sintering enhances the interfacial connections between nanoparticles, improving the electronic conductivity through the mesoporous network (Fig. S16). Concerning the cycle life and stability of the mesoporous structure annealed at high temperature (2100 nm diameter), the result at 5 C over 500 cycles (Fig. 6c) demonstrates a high retention of 86 and 81 % for the 500 and 600 °C annealed samples, respectively, with Coulombic efficiencies near to 100 % for both samples.

In another experiment, 800-nm-diameter beads with 25 nm pore size were annealed at different temperatures (from 300 to 650 °C) to further investigate the effect of annealing temperature on the electrochemical performance. All the XRD patterns (Fig. S12) can be indexed to the anatase phase, revealing a great stability of anatase phase within the annealed temperature range.[38] This result is also supported by the electron diffraction patterns (Fig. S13). The nitrogen gas sorption isotherms indicate that the mesoporous structures remained (Fig. S14a) and the BET surface area decreased with increasing annealing temperature (Table 3). Different from the 15 nm pore-sized beads (see Fig. S10 and S11b), the average pore size was stable at ~25 nm over this temperature range (Fig. S14b). However, the crystal size increased with increasing annealing temperature, as demonstrated by the estimated value from the XRD patterns and BET surface area (Table 3). In the galvanostatic experiment at 0.2 C rate, despite the loss of BET surface area and increase in crystal size, the MMTBs sustained a similar overall capacity upon increasing the annealing temperature (Fig. S15). Particularly, the MMTBs annealed at 650 °C showed slightly larger bulk capacity (region I and II), but this is offset by its smaller surface capacity (region III). The latter phenomenon is due to the large crystal size, that provides more octahedral sites inside the bulk anatase.[25] At high current rate (40 C), the poorer performance of the MMTBs annealed at 300 °C (Fig. 6d) can be ascribed to the organic content remaining in the beads from the synthesis, which may hinder the electrolyte diffusion and electron transfer. The beads annealed at 500 and 650 °C delivered similar rate capabilities of 45.5 and 44.1 mAh g^{-1} at 40 C rate, respectively (Fig. 6d and 6e). However, a different shape of the charge voltage profiles (Fig. 6e) is observed, showing that the sample annealed at 650 °C has smaller bulk capacity (Regions I and II) than that of the 500 °C sample, thus suggesting a lithium diffusion limitation for the 650 °C annealed sample due to its relatively large crystal size. The enhancement of the performance at high current is correlated to the reduction in the charge transfer resistance as a result of the increase in annealing temperature, as clearly suggested by the corresponding EIS plots shown in Fig. 6f. In contrast, the diffusion coefficients estimated from the EIS data showed only slight variation in the same order of magnitude (Table S2).

Table 3. Physical properties of the 800 nm anatase beads featuring a 25 nm mesopore and annealed at different temperatures for 2 h in air

Temperature (°C)	Crystal size[a] (nm)	Surface area (m^2 g^{-1})	Pore diameter[b] (nm)
650	17.6	63	25
500	15.8	85	25
400	15.5	91	25
300	15.5	94	25

[a)]Determined by applying Scherrer equation to (101) anatase peak of the corresponding XRD pattern.

[b)]Calculated using the BJH model on the N_2 adsorption branch.

The outstanding electrochemical performance of these materials is largely due to their mesoporous structure which can ensure close contact between the Li^+ ions and the primary anatase nanoparticles within the MMTBs. These results demonstrate that the rate capability of the bead materials can be effectively improved by enhancing the inter-particle bonding within/between the spherical particles. For the largest mesoporous beads (~2100 nm diameter), however, there is ultimately a limit to enhance their electronic conductivity within the bead, not only due to the intrinsic semiconductor property of anatase, but also due to the greater number of crystal boundaries that comprise the electronic pathway. Thus despite the improvements accessed through careful sintering between the primary anatase nanoparticles,[39, 40] the largest beads still present a relatively large number of crystal interfaces/boundaries and hence a long path length that the electrons have to travel. This limits the utilization of the inner parts of the MMTBs, thus weakening the electrochemical performance at the high currents. Fig. 7 illustrates the different electron conduction environments in the electrodes prepared using MMTBs annealed at different temperatures. Fig. 7a shows the interaction of the MMTBs with the current collector and the conductive carbon black embedded in liquid electrolyte (represented by the yellow background). Near to the outer surface of the MMTBs, the electron pathway is through a few nanoparticle boundaries, as represented in Fig. 7b. However, deep inside the MMTBs, the electron pathway is more tortuous because a greater number of boundaries need to be passed, as depicted in Fig. 7c. Increasing the annealing temperature results in improved sintering between the anatase nanoparticles (Fig. S16), leading to an enhanced electron transfer (illustrated in Fig. 7d) within the MMTBs.

Moreover, the XPS analyses indicated a comparable surface chemistry of the synthesised MMTBs (Fig. S17-S19), assuring a fair comparison between the MMTBs.

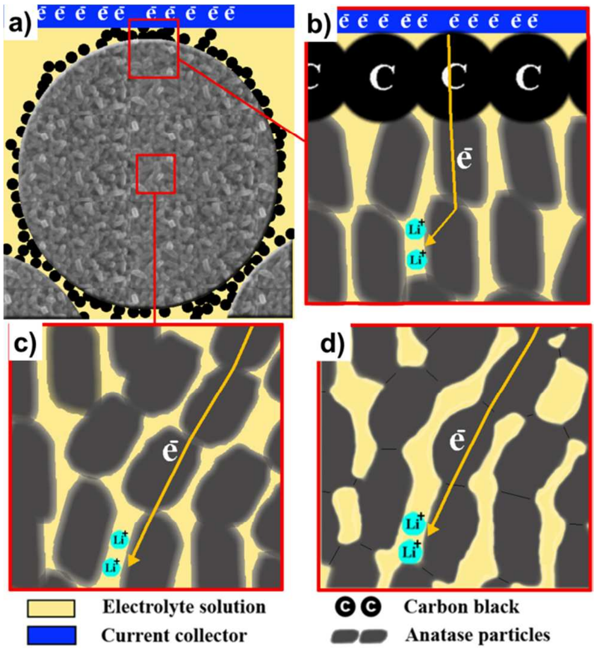

Fig. 7. Illustrations of the different electron conduction pathways in the electrodes prepared using MMTBs annealed at different temperatures. a) Anatase nanocrystals have different surrounding environments (with/without surrounding conductive carbon nanoparticles). b) Electron pathway near the outer interface of the MMTB. c) Electron pathway through the interior of the MMTB with abundant inter-particle boundaries. d) Enhanced electron conduction through the well-interconnected networks within the MMTB annealed at a relatively high temperature.

Conclusions

The influence of the physical properties of a series of mesoporous anatase beads on their electrochemical performance was investigated by systematically varying the pore diameter, bead diameter and sintering temperature. Comparing MMTBs with mesopore sizes of 15 and 25 nm, there was no direct limitation on electrolyte diffusion related to the pore size, but there was a direct effect on the discharge capacity that relates to the specific surface area and hence the crystal size of the primary nanoparticles. For varying the bead diameter, the optimal amount of conductive carbon required in the electrode was proved to be a function of the average diameter of the mesoporous bead. Tailoring of bead diameter allows minimisation of the fraction of conductive additive, thereby maximizing the energy density of the resultant electrodes. For the larger beads with a diameter of 2100 nm, the reduced performance at high current density is associated with the limited internal electron conductivity. This can be improved by increasing the annealing temperature. Overall, the electrochemical performance of these MMTBs shows that they are excellent anode candidates that can deliver high discharge capacity at high current densities, while also showing long charge/discharge cycling ability, due to the inherent structural stability of the mesoporous networks within the beads.

Acknowledgements

The authors acknowledge support from the Particulate Fluids Processing Centre, CSIRO for the OCE Science Leader Scheme and the Melbourne Advanced Microscopy Facility for access to electron microscopy facilities. R. A. C. acknowledges the Australian Research Council for a Future Fellowship (FT0990583).

References

1. Y. Tang, Y. Zhang, W. Li, B. Ma and X. Chen, *Chem. Soc. Rev.*, 2015, **44**, 5926-5940.
2. T. H. Kim, J. S. Park, S. K. Chang, S. Choi, J. H. Ryu and H. K. Song, *Adv. Energy Mater.*, 2012, **2**, 860-872.
3. S. J. Harris, A. Timmons, D. R. Baker and C. Monroe, *Chem. Phys. Lett.*, 2010, **485**, 265-274.
4. Q. Wang, P. Ping, X. Zhao, G. Chu, J. Sun and C. Chen, *J. Power Sources*, 2012, **208**, 210-224.
5. Z. Chen, Y. Qin, Y. Ren, W. Lu, C. Orendorff, E. P. Roth and K. Amine, *Energy Environ. Sci.*, 2011, **4**, 4023-4030.
6. Z. Chen, I. Belharouak, Y. K. Sun and K. Amine, *Adv. Funct. Mater.*, 2013, **23**, 959-969.
7. G. N. Zhu, Y. G. Wang and Y. Y. Xia, *Energy Environ. Sci.*, 2012, **5**, 6652-6667.
8. Y. Tang, Y. Zhang, J. Deng, J. Wei, T. Hong Le, B. K. Chandran, Z. Dong, Z. Chen and X. Chen, *Adv. Mater.*, 2014, **26**, 6111-6118.
9. Y. Tang, Y. Zhang, J. Deng, D. Qi, W. R. Leow, J. Wei, S. Yin, Z. Dong, R. Yazami, Z. Chen and X. Chen, *Angew. Chem., Int. Ed.*, 2014, **53**, 13488-13492.
10. P. G. Bruce, B. Scrosati and J. M. Tarascon, *Angew. Chem, Int. Ed.*, 2008, **47**, 2930-2946.
11. K. Saravanan, K. Ananthanarayanan and P. Balaya, *Energy Environ. Sci.*, 2010, **3**, 939-948.
12. H. M. Xie, R. S. Wang, J. R. Ying, L. Y. Zhang, A. F. Jalbout, H. Y. Yu, G. L. Yang, X. M. Pan and Z. M. Su, *Adv. Mater.*, 2006, **18**, 2609-2613.
13. Q. Wang, H. Li, L. Chen and X. Huang, *Carbon*, 2001, **39**, 2211-2214.
14. C. Sun, S. Rajasekhara, J. B. Goodenough and F. Zhou, *J. Am. Chem. Soc.*, 2011, **133**, 2132-2135.
15. J. R. Ying, C. Y. Jiang and C. R. Wan, *J. Power Sources*, 2004, **129**, 264-269.
16. Q. Wang, H. Li, L. Q. Chen and X. J. Huang, *Solid State Ionics*, 2002, **152**, 43-50.
17. Z. X. Lin, M. B. Zheng, B. Zhao, G. Wang, L. Pu and Y. Shi, *J. Solid State Electrochem.*, 2014, **18**, 1673-1681.
18. J. Wang, Y. Zhou, Y. Hu, R. O'Hayre and Z. Shao, *J. Phys. Chem. C*, 2011, **115**, 2529-2536.
19. Y. Ma, G. Ji, B. Ding and J. Y. Lee, *J. Mater. Chem.*, 2012, **22**, 24380-24385.
20. H. B. Wu, X. W. Lou and H. H. Hng, *Chem. - Eur. J.*, 2012, **18**, 2094-2099.
21. J. S. Chen, Y. L. Tan, C. M. Li, Y. L. Cheah, D. Luan, S. Madhavi, F. Y. C. Boey, L. A. Archer and X. W. Lou, *J. Am. Chem. Soc.*, 2010, **132**, 6124-6130.
22. D. Chen, F. Huang, Y.-B. Cheng and R. A. Caruso, *Adv. Mater.*, 2009, **21**, 2206-2210.

23. D. Chen, L. Cao, F. Huang, P. Imperia, Y.-B. Cheng and R. A. Caruso, *J. Am. Chem. Soc.*, 2010, **132**, 4438-4444.
24. L. Cao, D. Chen and R. A. Caruso, *Angew. Chem., Int. Ed.*, 2013, **52**, 10986-10991.
25. C. Jiang, M. Wei, Z. Qi, T. Kudo, I. Honma and H. Zhou, *J. Power Sources*, 2007, **166**, 239-243.
26. P. Kubiak, T. Froschl, N. Husing, U. Hormann, U. Kaiser, R. Schiller, C. K. Weiss, K. Landfester and M. Wohlfahrt-Mehrens, *Small*, 2011, **7**, 1690-1696.
27. J. Y. Shin, D. Samuelis and J. Maier, *Adv. Funct. Mater.*, 2011, **21**, 3464-3472.
28. Y. Ren, L. J. Hardwick and P. G. Bruce, *Angew. Chem., Int. Ed.*, 2010, **122**, 2624-2628.
29. M. Wagemaker, G. J. Kearley, A. A. van Well, H. Mutka and F. M. Mulder, *J. Am. Chem. Soc.*, 2002, **125**, 840-848.
30. M. Wagemaker, R. van de Krol, A. P. M. Kentgens, A. A. van Well and F. M. Mulder, *J. Am. Chem. Soc.*, 2001, **123**, 11454-11461.
31. W. J. H. Borghols, D. Lutzenkirchen-Hecht, U. Haake, E. R. H. van Eck, F. M. Mulder and M. Wagemaker, *Phys. Chem. Chem. Phys.*, 2009, **11**, 5742-5748.
32. K. Zhu, Q. Wang, J. H. Kim, A. A. Pesaran and A. J. Frank, *J. Phys. Chem. C*, 2012, **116**, 11895-11899.
33. J. Jamnik and J. Maier, *Phys. Chem. Chem. Phys.*, 2003, **5**, 5215-5220.
34. J. Wang, J. Polleux, J. Lim and B. Dunn, *J. Phys. Chem. C*, 2007, **111**, 14925-14931.
35. F. Zhang, Y. Zhang, S. Y. Song and H. J. Zhang, *J. Power Sources*, 2011, **196**, 8618-8624.
36. K. X. Wang, M. D. Wei, M. A. Morris, H. S. Zhou and J. D. Holmes, *Adv. Mater.*, 2007, **19**, 3016-3020.
37. K. Park, Q. Zhang, D. Myers and G. Cao, *ACS Appl. Mater. Interfaces*, 2013, **5**, 1044-1052.
38. X. Wang, L. Cao, D. Chen and R. A. Caruso, *ACS Appl. Mater. Interfaces*, 2013, **5**, 9421-9428.
39. F. Sauvage, D. H. Chen, P. Comte, F. Z. Huang, L. P. Heiniger, Y. B. Cheng, R. A. Caruso and M. Graetzel, *ACS Nano*, 2010, **4**, 4420-4425.
40. F. Z. Huang, D. H. Chen, Q. Li, R. A. Caruso and Y. B. Cheng, *Appl. Phys. Lett.*, 2012, **100**, 123102.